Protoplanetary Disk Structures in Ophiuchus II: Extension to Fainter Sources

Sean M. Andrews[1,2], D. J. Wilner[1], A. M. Hughes[1], Chunhua Qi[1], and C. P. Dullemond[3]

sandrews@cfa.harvard.edu

ABSTRACT

We present new results from a significant extension of our previous high angular resolution ($0\rlap{.}''3 \approx 40\,\mathrm{AU}$) Submillimeter Array survey of the $340\,\mathrm{GHz}$ ($880\,\mu\mathrm{m}$) thermal continuum emission from dusty circumstellar disks in the $\sim 1\,\mathrm{Myr}$-old Ophiuchus star-forming region. An expanded sample is constructed to probe disk structures that emit significantly lower millimeter luminosities (hence dust masses), down to the median value for T Tauri stars. Using a Monte Carlo radiative transfer code, the millimeter visibilities and broadband spectral energy distribution for each disk are simultaneously reproduced with a two-dimensional parametric model for a viscous accretion disk that has a surface density profile $\Sigma \propto (R/R_c)^{-\gamma} \exp\left[-(R/R_c)^{2-\gamma}\right]$. We find wide ranges of characteristic radii ($R_c = 14\text{-}198\,\mathrm{AU}$) and disk masses ($M_d = 0.004\text{-}0.143\,\mathrm{M_\odot}$), but a narrow distribution of surface density gradients ($\gamma = 0.4\text{-}1.1$) that is consistent with a uniform value $\langle\gamma\rangle = 0.9 \pm 0.2$ and independent of mass (or millimeter luminosity). In this sample, we find a correlation between the disk luminosity/mass and characteristic radius, such that fainter disks are both smaller and less massive. We suggest that this relationship is an imprint of the initial conditions inherited by the disks at their formation epoch, compare their angular momenta with those of molecular cloud cores, and speculate on how future observations can help constrain the distribution of viscous evolution timescales. No other correlations between disk and star properties are found. The inferred disk structures are briefly compared with theoretical models for giant planet formation, although resolution limitations do not permit us to directly comment on material inside $R \approx 20\,\mathrm{AU}$. However, there is some compelling evidence for the evolution of dust in the planet formation region: 4/17 disks in the sample show resolved regions of significantly reduced millimeter optical depths within $\sim 20\text{-}40\,\mathrm{AU}$ of their central stars.

Subject headings: accretion, accretion disks — circumstellar matter — planetary systems: protoplanetary disks — solar system: formation — stars: pre-main-sequence

[1]Harvard-Smithsonian Center for Astrophysics, 60 Garden Street, Cambridge, MA 02138

[2]Hubble Fellow

[3]Max Planck Institut für Astronomie, Königstuhl 17, 69117 Heidelberg, Germany

1. Introduction

Direct observations of the reservoirs of planet-building material − the disks around young stars − should play a critical role in developing theoretical models of planet formation. Ultimately, the goal of those models is to elucidate the physical processes involved in making planets by incorporating the observed properties of circumstellar disks and successfully reproducing the demographic characteristics of the planets in our Solar System and those around other stars (e.g., Ida & Lin 2004; Mordasini et al. 2009). Regardless of the favored mechanism, two basic requirements for forming planets in a circumstellar disk must be satisfied: there must be enough material (gas and dust) in the right locations and a sufficient amount of time for the formation mechanism to operate (e.g., Pollack et al. 1996; Boss 1997). The former criterion amounts to a density threshold, suggesting that observational constraints on the spatial distribution of mass in young circumstellar disks are fundamental in constructing an empirical foundation for planet formation models. Moreover, those same estimates of disk densities can be used to help characterize the viscous accretion process that determines how disk structures evolve (e.g., Hartmann et al. 1998).

There are some significant observational obstacles to direct measurements of disk densities. Most of the material in these disks is "dark," composed of cold molecular hydrogen and not readily detectable. Their mass contents must be inferred from trace species, particularly from the dust grains that dominate the disk opacity. At radio wavelengths, the thermal continuum emission from these dust grains is optically thin and therefore provides an unique probe of mass in the disk midplane (Beckwith et al. 1990). If that emission can be resolved, properly interpreted with radiative transfer calculations, and assigned some nominal gas-to-dust mass ratio, it can be used to reconstruct the spatial distribution of disk densities. Interferometric observations of dust and trace gas species have helped quantify densities in the outer parts of circumstellar disks (Kitamura et al. 2002; Andrews & Williams 2007a; Hughes et al. 2008; Isella et al. 2009), clearly established the presence of vertical temperature and density gradients (Dartois et al. 2003; Piétu et al. 2007), and even identified disks with large central cavities that exhibit very little dust emission (Piétu et al. 2006; Hughes et al. 2007, 2009; Brown et al. 2008, 2009; Isella et al. 2010).

In a previous study (Andrews et al. 2009, hereafter Paper I), we presented the initial part of a high angular resolution ($0\farcs3 \approx 40\,\mathrm{AU}$) survey of the $880\,\mu$m thermal dust emission from protoplanetary disks in the nearby Ophiuchus star-forming region. To take advantage of these observations that are sensitive to the mass content inside the planet formation zone ($R \leq 40\,\mathrm{AU}$), we developed a radiative transfer modeling toolkit to extract the two-dimensional temperature and density structures of these disks through a combined fit of their millimeter continuum visibilities and broadband spectral energy distributions (SEDs). Through that modeling effort, we concluded that the disks had densities comparable to those expected for the outer parts of the primordial disk around the Sun and very similar radial density gradients. The inferred density gradients indicate that whatever mechanism is responsible for generating viscosity in these disks acts with a nearly linear radial distribution (i.e., the viscosities vary as $\nu \propto R^{\gamma}$, with a median $\gamma \approx 0.9$). Moreover, we resolved large regions ($R \approx 20\text{-}40\,\mathrm{AU}$) with very little millimeter emission in the centers of several

disks, and speculated that these may be the signposts of young planetary systems. However, that initial sample was biased towards the targets that are exceptionally bright at millimeter wavelengths, and therefore considerably more massive than the typical disk in the Ophiuchus region (see Andrews & Williams 2007b). In this article, we extend the survey to double the sample and probe disk structures with millimeter luminosities down to the median value for $\sim$1 Myr-old T Tauri stars. In §2 we describe the sample selection criteria, new observations, and data calibration. A brief review of the radiative transfer calculations is provided in §3, with the modeling results for this extension of the sample highlighted in §4. In §5, we synthesize the disk structure constraints for the full sample in the contexts of the viscous evolution process and the prospects for planet formation. The key conclusions from the survey are summarized in §6.

2.   Sample Selection, Observations, and Data Reduction

The sample of disk targets for this survey was selected primarily for observational and analytical convenience. To ensure that the SMA data would be sufficiently sensitive to probe emission over a large range of spatial scales, targets were required to have integrated $880\,\mu$m flux densities larger than $\sim$75 mJy. Candidates were selected based on the single-dish photometry compiled by Andrews & Williams (2007b). When no $880\,\mu$m data were available, we relied on the 1.3 mm flux densities provided by previous surveys (André & Montmerle 1994; Nürnberger et al. 1998) and conservatively scaled up by the square of the wavelength ratio ($\sim$2.2; see Andrews & Williams 2005b, 2007b). After this initial cut, we excluded targets that lacked sufficient information about their central stars. Without stellar temperatures and luminosities, it is not possbile to interpret the observed millimeter data in detail (see §3). In practice, this second criterion amounted to an extinction threshold $A_V \lesssim 15$, as spectral classifications and luminosity estimates are rare and uncertain for more deeply embedded sources (Luhman & Rieke 1999; Wilking et al. 2005; Furlan et al. 2009). The sample selection-space set by these criteria is shown in Figure 1, with red points marking the selected target disks. The $880\,\mu$m flux densities for those points correspond to the values derived from the SMA observations described here or in Paper I. One selected target, WL 18, falls below the designated millimeter emission threshold: previous 1.3 mm data led us to expect a larger $880\,\mu$m flux density than was observed. One other target, RX J1633.9$-$2422, meets the selection criteria but was not observed: its millimeter flux density was only recently published (Cieza et al. 2010).

These combined criteria yielded 17 disk targets for the sample. The $880\,\mu$m flux density criterion corresponds to the median value found in both the Ophiuchus and Taurus star-forming regions (Andrews & Williams 2005b, 2007b). Therefore, the sample defined here fully spans the upper half of the millimeter continuum luminosity distribution $-$ or equivalently the circumstellar dust mass distribution $-$ for the disks around $\sim$1 Myr-old stars. For the typical assumptions in converting this emission to total disk masses, this limit corresponds to a few Jupiter masses ($\sim$0.004 M$_\odot$) of gas and dust, suggesting that the sample is representative of the disk population that might eventually be able to produce giant planets. Moreover, the sample includes targets that

essentially span the full range of T Tauri star properties, including spectral types from M4 to G3, stellar masses of 0.3-2.0 $M_\odot$, and accretion rates of $\sim 10^{-9}$-$10^{-7}\,M_\odot\,\mathrm{yr}^{-1}$.

To complete this sample and expand on the initial 9 disks discussed in Paper I, 8 additional targets were observed with the very extended (V; 8-509 m baselines) and compact (C: 6-70 m baselines) configurations of the Submillimeter Array interferometer (SMA; Ho et al. 2004) in 2009 March and May. A journal of these SMA observations is provided in Table 1. The SMA double sideband receivers were tuned to a local oscillator (LO) frequency of 340.755 GHz (880 μm). Each sideband was divided into 24 partially overlapping 104 MHz chunks centered ± 5 GHz from the LO frequency. The central chunk in the upper sideband was sampled at a factor of 4 higher spectral resolution than the others, in an effort to observe the CO $J=3-2$ transition (345.796 GHz) in 0.70 km s^{-1} channels. The observing sequence interleaved disk targets with nearby quasars, J1625$-$254 and J1626$-$298, in an alternating pattern with a total cycle time of $\sim$10-15 minutes. When the targets were at low elevations ($<20°$), planets (Uranus, Saturn), satellites (Titan, Callisto), and bright quasars (3C 454.3, 3C 279) were observed as bandpass and absolute flux calibrators depending on their availability and the array configuration. The observing conditions were generally very good, with atmospheric opacities <0.1 at 225 GHz (corresponding to <2.0 mm of precipitable water vapor).

The data were edited and calibrated as in Paper I using the `MIR` software package. The bandpass response was calibrated with observations of a bright planet or quasar, and broadband continuum channels in each sideband were generated by averaging the central 82 MHz in all of the chunks except the one reserved for the CO $J=3-2$ line. The visibility amplitude scale was set based on observations of planets or satellites and routinely-monitored quasars: the typical systematic uncertainty in the absolute flux scale is $\sim$10%. The antenna-based complex gain response of the system as a function of time was determined with reference to J1625$-$254, which lies only $\sim 1°$ from the target disks. The other quasar in the observing cycle provides a check on the quality of the phase transfer in the gain calibration process. The millimeter "seeing" generated by atmospheric phase noise and any small baseline errors is small, 0.1-0$\overset{''}{.}$2. After combining all of the data for each target, the standard tasks of Fourier inverting the visibilities, deconvolution with the `CLEAN` algorithm, and restoration with a synthesized beam were conducted with the `MIRIAD` software package. High resolution maps of the continuum emission were created with a Briggs robust = 0.2-0.7 weighting scheme for the visibilities, and maps of the CO $J=3-2$ line emission were made with natural weighting for the compact array data only. The relevant data properties from these synthesized maps are compiled in Table 2.

The synthesized continuum maps for these targets are featured in Figure 2. Each high angular resolution map covers 4$''$ on a side, corresponding to 500 AU at the adopted distance of 125 pc to the Ophiuchus clouds (de Geus et al. 1989; Knude & Høg 1998; Lombardi et al. 2008; Loinard et al. 2008). A centroid position and initial estimate of the viewing geometry of the disk $-$ characterized by the inclination (i) and major axis position angle (PA) $-$ were determined by fitting the visibilities with an elliptical Gaussian brightness distribution. Because the continuum emission from the SR 24 system is not centrally peaked, its centroid position and viewing geometry were estimated by

inspection of the lower resolution (compact SMA configuration) data only. In all cases, the CO line emission from the disks is significantly contaminated by the local molecular cloud environment, and will not be discussed further.

3.   Modeling the Disk Structures

To interpret these observations in the context of the disk structures − physical conditions and key size scales − present in this sample, we followed the modeling formalism introduced and discussed in detail in Paper I. To briefly summarize that procedure, we first adopt a parametric prescription for a two-dimensional, flared density structure based on a simple model for the viscous evolution of an accretion disk (Lynden-Bell & Pringle 1974; Hartmann et al. 1998). The model assumes an anomalous disk viscosity that varies with radius as $\nu \propto R^\gamma$ and has a surface density profile

$$\Sigma = (2 - \gamma)\frac{M_d}{2\pi R_c^2}\left(\frac{R}{R_c}\right)^{-\gamma}\exp\left[-\left(\frac{R}{R_c}\right)^{2-\gamma}\right],\tag{1}$$

where R_c is a characteristic scaling radius and M_d is the disk mass. At a given radius, that column density is vertically distributed so that it falls off with altitude above the midplane like a Gaussian with scale-height $H \propto R^{1+\psi}$. Once a density structure has been specified with a set of five parameters, $\{M_d, \gamma, R_c, H_c, \psi\}$ (where H_c is the scale-height at the characteristic radius), it is populated with a spatially homogeneous size distribution of dust grains. As described in Paper I, we consider dust with an interstellar medium composition (Draine & Lee 1984; Weingartner & Draine 2001) and a power-law distribution of sizes (with an index of -3.5) between $0.005\,\mu$m and 1 mm. This dust structure is then irradiated by a central star of fixed temperature and luminosity to determine an internally-consistent disk temperature structure, using the two-dimensional Monte Carlo radiative transfer code `RADMC` (Dullemond & Dominik 2004). The results of the Monte Carlo simulation are then coupled with a post-processing raytracing code to compute a synthetic dataset for a given viewing geometry, consisting of both a broadband spectral energy distribution (SED) and a set of millimeter continuum visibilities that sample the Fourier plane in the same way as the SMA data. These synthetic data are simultaneously compared with the observations, and the process is iterated until the fit converges on a minimum joint χ^2 value (see Paper I for details).

The stellar properties used to generate the Kurucz spectra that irradiate the disk structures are listed in Table 3, based on both literature measurements and matches to the optical/near-infrared SED. Because the spatio-kinematic information from the CO line emission in these disks is sufficiently contaminated by the local cloud material, estimates of the disk inclinations and position angles were determined solely from the elliptical Gaussian fits to the continuum emission described in §2. Unfortunately, the relatively faint continuum signals from some of these targets leads to considerable uncertainty in these viewing geometry estimates. These are still the best values available, but we caution that some systematic uncertainty will remain for the density parameters until better emission line data are available for these targets. With such a limited amount of

spatially resolved information about the two components in the DoAr 24 E system, a detailed modeling of this source is beyond the scope of this study. Some important modifications to the modeling process were made for the SR 24 S disk, with the details provided in §4.2.

4. Results

4.1. Disk Structures

The model parameter values that best reproduce the observations for the full sample are compiled in Tables 4 and 5 for the disks with continuous emission distributions and those with central emission cavities, respectively. For the continuous disks, we include the (fixed) inner disk radii inferred from a simple sublimation argument (see Paper I; Table 4, column 7). Columns 7 and 8 in Table 5 list the estimated sizes (R_{cav}) and density contrasts (δ_{cav}) used to account for the disks with central emission cavities. Both tables also include the adopted values for the disk inclination and position angle, as well as the reduced χ^2 statistics for the fits to the SED and visibility datasets separately. The distributions of these values for each parameter are shown together in Figure 3; hatched regions mark contributions from the disks with central cavities (around SR 24 S, SR 21, DoAr 44, and WSB 60). In Figure 4, the new observations presented here are directly compared with the synthetic datasets generated from these best-fit models (see Paper I for the other sample disks). From left to right, we display the observed SMA millimeter continuum image (as in Figure 2), the synthesized model image, the imaged residuals, the broadband SED, and the elliptically averaged millimeter visibility profile (see Paper I for details). The latter two panels have the best-fit model behavior overlaid in red, and the SED panel also shows the input stellar spectrum as a dashed blue curve. Because of its large central emission cavity, the modeling results for the SR 24 S disk are shown separately in Figure 5, with inset images synthesized at higher angular resolution to facilitate a more detailed comparison.

The modeling uncertainties and relationships between the observations and model parameters were already discussed in detail in Paper I, so we will not repeat that effort here. Instead, we focus on how this expanded sample enables new constraints on the spatial distribution of mass in $\sim$1 Myr-old circumstellar disks. The inferred surface density profiles for the full sample are shown together in Figure 6, with the targets presented for the first time here highlighted in color. The disks with large central emission cavities are shown in a separate panel. The light gray band inside 20 AU marks the survey resolution limit, while the dark gray boxes are reference points representing the minimal surface densities (with uncertainties) and presumed feeding zones for Saturn, Uranus, and Neptune in the canonical model for the primordial solar disk (Weidenschilling 1977). Although the disks in this sample exhibit a wide range of masses (M_d; Figure 3a) and characteristic radii (R_c; Figure 3c), we find a very narrow distribution of values for γ, the radial gradient of the surface density profile. As shown in Figure 3b, that distribution is roughly normal with a peak at $\gamma = 0.9$ and a standard deviation of 0.2. Since that width is comparable to the modeling uncertainties on

γ for an individual source ($\sim$0.2-0.3; Paper I), the modeling results are consistent with a uniform γ value being representative of the entire sample.[1] Moreover, by extending the survey to cover much fainter targets, we have confirmed that the shape of the surface density profile does not significantly change over a wide range of millimeter luminosities (or disk masses).

Despite the similar radial density gradients in these disks, the observations clearly show a wide variety of millimeter emission morphologies. Some of that diversity is related to how the disks are heated by their central stars, a natural outcome of the assortment of stellar properties and vertical distributions of dust present in the sample (see Paper I for details). However, the density profiles plotted in Figure 6 demonstrate that a significant range of characteristic radii and masses are also partly responsible. A close examination of those Σ profiles reveals that the brighter disks at millimeter wavelengths tend to have both higher masses and larger characteristic radii. The former is no surprise, since the vast majority of the disk volume at these wavelengths is optically thin, but there is no *a priori* reason to expect the disk sizes to be correspondingly smaller for fainter sources. This relationship is not a modeling artifact, as there is an analogous empirical correlation between the brightness of the millimeter emission and how well that emission is resolved. Figure 7 demonstrates this explicitly by comparing the average $880\,\mu$m visibility profiles for disks that are brighter (*red*) or fainter (*blue*) than 0.5 Jy. These profiles were calculated by averaging the visibilities for each subset of disks into annular bins, after deprojecting the visibilities for individual disks according to their viewing geometries and normalizing their real (correlated) fluxes by dividing off their integrated flux densities. This comparison confirms that the millimeter emission from the brighter disks in this sample is more resolved by our SMA data, exhibiting substantially less correlated flux on essentially all spatial scales. Although the physical origins of this empirical relationship are not obvious, some speculations about its significance for understanding the viscous evolution process in these disks are presented in §5.

In an effort to identify any trends among the disk structures or the characteristics of their stellar hosts, we performed a principle component analysis on a subset of such properties for the 12 disks with continuous density distributions in this sample. The analysis included the 5 free disk structure parameters, $\{M_d, \gamma, R_c, H_{100}, \psi\}$, the stellar properties $\{T_{\text{eff}}, L_*\}$, and the accretion rates, $\dot{M}_*$ (see Tables 3, 4, and 6). Due to the additional uncertainties of the stellar evolution models used to infer them, we did not include stellar ages, masses, or radii directly (although those values are well-correlated with L_* and T_{eff}). As alluded to above, we identified one statistically significant correlation ($3.3\,\sigma$; correlation coefficient of 0.85) between M_d and R_c, which will be discussed in detail in §5.1. The first eigenvector from the principle component analysis, accounting for 40% of the variance in the data, is dominated by a positive trend relating R_c, M_d, L_*, and $\dot{M}_*$. The trend indicates that the more massive disks in this sample are larger and orbiting more luminous - perhaps younger - stars that are accreting disk material at higher rates. While these relationships

---

[1]The only major outlier, the disk around AS 209, has a particularly uncertain γ estimate due to a poorly-sampled infrared SED (see Paper I for details).

may hint at crucial information related to the viscous evolution process, a larger sample will be required to make any definitive conclusions.

4.2. Commentary on Individual Disks

Elias 24 – This heavily-reddened classical T Tauri star is one of the brightest millimeter continuum sources in Ophiuchus. In fact, it was initially excluded from the sample out of concern that the bright emission signaled contamination from an extended envelope. However, there is no evidence for the spatial filtering of such large-scale emission; the SMA flux densities at both $880\,\mu$m and $1.3\,$mm are in excellent agreement with lower resolution single-dish photometry (Andrews & Williams 2007a,b; André & Montmerle 1994). Moreover, the central star is optically visible (Wilking et al. 2005) and the infrared SED shape is incompatible with a substantial envelope (Bontemps et al. 2001; Evans et al. 2003; Barsony et al. 2005). The $880\,\mu$m continuum data presented here features a bright central core and a fainter, extended, and apparently asymmetric emission halo on larger scales. Although the best-fit model for this source is able to reproduce the SED and visibilities rather well, any axisymmetric model will underpredict the extended emission to the east of the disk center at the $\sim3\sigma$ level (see Figure 4). The origins of that extension remain unclear.

SR 24 S – The hierarchical triple system SR 24 is composed of this K2 star and a close binary pair ($0\farcs2 \approx 25\,$AU; Simon et al. 1995) located $\sim5''$ ($625\,$AU) to the north (Reipurth & Zinnecker 1993). Both SR 24 S and the SR 24 N binary exhibit excess emission from warm dust disks, bright Hα lines indicative of substantial accretion flows, and extended emission from CO low-energy rotational transitions. However, all of the continuum emission at millimeter wavelengths is produced by SR 24 S (Andrews & Williams 2005a; Patience et al. 2008; Isella et al. 2009). The high angular resolution inset image of the SR 24 S disk in Figure 2 reveals a resolved central emission cavity with an apparent brightness enhancement to the northeast. The origins of this ring-like emission morphology are unclear, but could perhaps be generated by abrupt emissivity variations due to particle growth, a dramatic dissipation process driven by high-energy radiation from the star, or even tidal interactions with companion objects (in this last case, see Mayama et al. 2010).

Regardless of the cause, the model described in §3 was adjusted to account for the observed disk morphology. As detailed in Paper I for similar cases, we adopted the simple modification of artificially decreasing the surface densities inside a radius $R_{\rm cav}$ by a factor $\delta_{\rm cav}$ and then attempted to fit the SMA visibilities and the component-resolved optical (Wilking et al. 2005), infrared (Jensen & Mathieu 1997; Cutri et al. 2003; Evans et al. 2003; McCabe et al. 2006), and radio photometry. However, much like the case of the DoAr 44 disk described in Paper I, it is difficult to simultaneously account for the significant infrared excess and the lack of millimeter continuum emission near the SR 24 S stellar position. Following the approach of Espaillat et al. (2007) for other "pre-transitional" disks, we proceeded by first finding a good match to the millimeter visi-

bilities, and then artificially increasing the surface densities near the star until sufficient infrared emission was produced to match the SED (without affecting the millimeter emission). A satisfactory result was achieved with a surface density profile scaled down by $\delta_{\mathrm{cav}} \approx 0.05$ inside $R = 2\,\mathrm{AU}$, a factor of 20 lower than for a continuous disk, but $\sim 500\times$ higher than for the region between $2\,\mathrm{AU}$ and $R_{\mathrm{cav}} \approx 32\,\mathrm{AU}$. Obviously these adjustments are artificial and non-unique; a modeling effort focused on a more robust exploration of the detailed inner disk structures will be treated elsewhere.

SR 4 – This star harbors a disk with a compact, centrally-peaked millimeter emission morphology. The low foreground extinction allows for a particularly good characterization of the stellar luminosity from optical photometry, despite the low-level variability at those wavelengths (Herbst et al. 1994). The infrared SED shows a relatively small excess at short wavelengths before a pronounced flattening from $\sim$8-24 μm (Cutri et al. 2003; Evans et al. 2003). Unfortunately there is little additional information in the far-infrared to better constrain the SED morphology, as the *Spitzer* 70 μm images are contaminated by local nebulosity (Padgett et al. 2008). This lack of data between the mid-infrared and millimeter regions of the SED results in only a relatively crude constraint on the vertical structure parameters (and thus temperatures) in this case.

SR 13 – Another hierarchical triple system (see Schaefer et al. 2006), SR 13 includes a close binary pair (13 mas $\approx 1.6\,\mathrm{AU}$; Simon et al. 1995) and a tertiary companion located $\sim 0\!\!''\!4$ (50 AU) due east (Ghez et al. 1993). Lacking sufficient component-resolved photometry for this system, we made a preliminary model ignoring the tertiary and assuming the primary is a single star. The SED was constructed from the composite optical measurements of Herbst et al. (1994), infrared data from 2MASS and the *Spitzer* c2d survey (Cutri et al. 2003; Evans et al. 2003), and single-dish radio observations (André & Montmerle 1994; Andrews & Williams 2007b). Despite this simplification, the SMA data can potentially resolve another disk around the tertiary. There is a modest eastern extension in the emission map, and a potential null near 400 kλ in the deprojected visibility profile (Figure 4). These features could be produced either by a cavity in a circum-system disk or by a marginally resolved additional disk around the spatially offset tertiary. With the available sensitivity, it is difficult to differentiate these scenarios. Needless to say, the model disk structure inferred in this case should be treated with appropriate caution.

WSB 52 – This classical T Tauri star with spectral type M1 exhibits a compact millimeter continuum emission distribution typical of the fainter disks in the sample. The SED used in the model fits was constructed from the red-optical photometry of Wilking et al. (2005), infrared measurements from 2MASS (Cutri et al. 2003), *Spitzer* c2d (Evans et al. 2003), and Padgett et al. (2008), and a 1.3 mm single-dish flux measurement from Stanke et al. (2006).

DoAr 33 – The infrared excess emission around this K4 star is remarkably faint compared to the typical young disk. We constructed a SED from red-optical photometry (Wilking et al.

2005), the 2MASS and *Spitzer* c2d programs (Cutri et al. 2003; Evans et al. 2003), and single-dish radio measurements (André & Montmerle 1994; Andrews & Williams 2007b). Only a very weak continuum excess is present shortward of $\sim 8\,\mu$m. At longer wavelengths where the dust excess is brighter, the spectrum is very steep and blue. Reproducing this infrared SED shape with our models required the use of a very flat vertical distribution of dust, resulting in comparatively cold midplane temperatures. Cieza et al. (2010) argue that these infrared colors are indicative of significant dust evolution. The flat structure inferred here could be interpreted in that context as evidence for advanced dust sedimentation to the midplane, or perhaps the sign of extensive shadowing of the outer disk due to some perturbed inner disk structure. In any case, the coupling of the rare infrared SED, bright millimeter emission, and weak signatures of accretion (Cieza et al. 2010) suggest that this disk is worthy of further scrutiny.

WL 18 – This star harbors the faintest disk in the sample, due in part to its small size ($R_c = 14\,$AU). Its visibility profile shows that the millimeter emission is only marginally resolved on the longest SMA baselines. The SED compiled here is sparse due to high foreground extinction, with infrared data from 2MASS and the *Spitzer* c2d project (Cutri et al. 2003; Evans et al. 2003), and a single-dish 1.3 mm flux density measured by Motte et al. (1998). That same extinction makes an estimate of the underlying stellar luminosity difficult, which in turn contributes an uncertainty to the thermal structure of the disk. The apparently low luminosity of the star relative to others with the same spectral type (K7) leads to an uncomfortably large age estimate (11 Myr).

DoAr 24 E – This spectral type G6 weak-lined T Tauri star has a companion roughly $2''$ to the southeast (Ghez et al. 1993; Reipurth & Zinnecker 1993) that becomes substantially brighter than the primary at wavelengths longer than $\sim 3\,\mu$m (e.g., McCabe et al. 2006). The unresolved composite SED has been attributed to the photosphere of the primary and dust around this infrared companion. However, resolved measurements at near- and mid-infrared wavelengths (Prato et al. 2003; Barsony et al. 2005; McCabe et al. 2006) indicate that the primary does show some very weak infrared excess at least at $\sim 10\,\mu$m. Regardless, most of the unresolved millimeter emission, and therefore the circumstellar dust mass, was assumed to be generated by the infrared companion (Motte et al. 1998; Andrews & Williams 2007b). The resolved $880\,\mu$m image of this system in Figure 2 clearly demonstrates that this is not the case: each stellar component hosts a dust disk with roughly equal amounts of millimeter emission. Neither individual disk is clearly resolved. The composite and component-resolved SEDs for this system are shown together in Figure 8, along with a potential model for an extincted stellar photosphere from the primary. Since very little resolved information is available and the nature of the infrared companion is uncertain, we have not modeled the circumstellar material in this system. There is potentially great interest in doing so with some modifications to the standard technique presented here. It would be worthwhile to better understand the lack of accretion onto the primary despite the presence of a substantial dust mass, as well as the potential origin of the very red SED of the companion object.

5. Discussion

5.1. Constraints on Viscous Evolution

We have used a radiative transfer modeling technique to extract the dust density structures for a significant sample of protoplanetary disks based on high angular resolution observations of their millimeter continuum emission. Those data and the SEDs for each source were reproduced well using a simple model for the two-dimensional density structure of a viscous accretion disk, with a parametric surface density profile that varies with radius like a power-law with an exponential taper at large radii (see Eq. [1]). This specific form of Σ corresponds to the Lynden-Bell & Pringle (1974) similarity solutions for the evolution of a thin accretion disk in Keplerian rotation around a (stellar) point mass, with a viscosity $\nu \propto R^\gamma$ that does not vary with time (see also Hartmann et al. 1998). This type of model - without a sharply truncated outer edge - is favored observationally, as it provides a natural explanation for the optical absorption profiles of silhouette disks in Orion (McCaughrean & O'Dell 1996) and reconciles the apparent discrepancies in the observed spatial extents of the dust and CO line emission for nearby resolved disks (Hughes et al. 2008).

In the context of these models, Figure 3b demonstrates that there is a relatively narrow distribution of the parameter γ that describes the spatial distribution of mass in the disk, consistent with a median $\langle \gamma \rangle = 0.9 \pm 0.2$ when the sample is considered together (estimates for individual disks range from $\gamma = 0.4$-1.1). These values fall at the high end of the wider distribution of Σ gradients inferred by Isella et al. (2009, where γ ranges from -0.8 to 0.8) using a 1.3 mm continuum survey of Taurus disks with slightly poorer angular resolution (0.7-1.0″), and therefore probing the mass at larger disk radii. Although there is substantial overlap in the γ distributions from both surveys (particularly when the disks with large central cavities are ignored), the differences can be attributed to the distinct approaches for interpreting the data and there is no obvious means of reconciliation at present. Focusing on our results, we infer that the mass in ∼1 Myr-old disks has a similar radial distribution regardless of the wide range of total masses ($M_d \approx 0.001$-0.1 $M_\odot$) probed in this sample. This implies that whatever mechanism is responsible for generating the viscosity in these disks insures that it has a roughly linear dependence on radius ($\gamma \approx 1$).

Since the physical origin of that viscosity is unclear, we adopt a simple prescription $\nu = \alpha c_s H$, where c_s is the sound speed and the viscosity coefficient α describes the efficiency of the angular momentum transport (Shakura & Sunyaev 1973). Using the density structures and measurements of mass accretion rates $\dot{M}_*$ (see Table 6 for references), we can estimate the value of the viscosity coefficient $\alpha(R) \approx \dot{M}_*(R/R_c)^\gamma/3\pi\Sigma_c c_s H$ (see the Appendix in Paper I for details). The resulting distribution of α at $R = 10$ AU is shown in Figure 9, with values for individual disks listed in Table 6. Note that for the typical midplane temperature distribution $T \propto R^{-q}$, the viscosity coefficient is proportional to $R^\gamma/c_s H \sim R^z$, where $z \approx \gamma + q/2 - \psi - 1$. The model parameters and temperature distributions inferred for this sample have $z \approx 0.0 \pm 0.3$, meaning α does not vary by more than a factor of ∼2-4 across the disk. The inferred distribution of these viscosity coefficients appears bimodal, with peaks just below $\alpha \approx 0.001$ and above 0.01. However, given

the small sample, those peaks are not statistically significant; they simply represent the clustering of the accretion rates in this sample. The range of inferred α values is in reasonable quantitative agreement with magnetohydrodynamics simulations where the viscosity is generated by turbulence from the magnetorotational instability in slightly ionized disks (Hawley et al. 1995; Stone et al. 1996; Fleming & Stone 2003; Fromang et al. 2007). However, we should caution that these α values are not yet well constrained: they suffer the combined uncertainties in the accretion rates and disk structure parameters, as well as from systematic issues with the inherent assumptions in their derivation (e.g., the dust traces the gas, viscous heating is insignificant, etc.). They represent only a first exploration of an improved empirical understanding of disk viscosities.

The interactions of gravitational and viscous torques control the evolution of disk structure over the vast majority of the disk lifetime. This viscous evolution process has two important, observable effects on that structure. First, the coupling of the viscosity and the Keplerian orbital shear drives a net mass flow toward small radii, where material can be magnetically channeled onto the central star. That mass flow produces bright H emission lines, and the shock generated when it impacts the stellar surface gives rise to a strong ultraviolet continuum; both tracers can be used to estimate $\dot{M}_*$ (Muzerolle et al. 1998a,b; Gullbring & Calvet 1998; Gullbring et al. 2000). To compensate for the angular momentum dissipated in that process, the material in the outer disk (beyond some radius R_t; see Table 6 and Paper I) is spread to larger radii. The results of that viscous diffusion - decreased average densities (i.e., M_d) and increased sizes (R_c) - can be probed with resolved observations of the millimeter continuum emission. In principle, tracking these observational signatures as a function of time could provide strong constraints on the viscous evolution process. Isella et al. (2009) claim a significant correlation between their parameterization of R_c and stellar age in a sample of Taurus disks. No such correlation is evident in our larger sample of Ophiuchus disks. More importantly, the search for such a trend within a single star-forming region is probably premature; the ages of individual young stars can not be determined with sufficient accuracy to infer such evolutionary behavior (e.g., Hillenbrand 2009, and references therein), even though it may exist. Rather, the inferred disk structures could be considered representative of the diversity of evolutionary states and/or initial conditions at a "snapshot" in the evolution sequence corresponding to some median cluster age (in this case, $\sim 1\,\mathrm{Myr}$).

While there may not be much difference in the shapes of the Σ profiles (γ), this sample includes disks with a wide variety of masses (M_d) and characteristic size scales (R_c). As was demonstrated in Figure 7, the disks with brighter millimeter emission have systematically larger masses *and sizes*. This relationship is illustrated more directly in Figure 10, with a significant correlation ($3.3\,\sigma$; Spearman rank coefficient of 0.85) between R_c and M_d that can be approximated as a power-law, $M_d \propto R_c^{1.6\pm0.3}$. The physical origin of the correlation is not clear. One potential explanation is that it reflects the range of initial conditions and viscous properties inherited at the disk formation epoch. In that case, note that the sense of the correlation is almost perpendicular to the evolutionary paths for individual disks that conserve angular momentum, $M_d \propto R_c^{-1/2}$. The spread along the correlation is then representative of the distribution of angular momenta imparted by the collapse of

the parent molecular cloud cores. Following Isella et al. (2009), we can estimate the specific angular momenta in these cores that are needed to reproduce the inferred disk structures. Assuming the centrifugal radius in the disk corresponds to the radius that contained $\sim 90\%$ of the disk mass at the formation epoch (here defined as approximately twice an initial scaling radius, $\sim 2R_1$), then the specific angular momentum can be written

$$j \approx 2 \times 10^{20} \left(\frac{R_1}{25\,\mathrm{AU}} \right)^{0.5} \left(\frac{M_*}{\mathrm{M_\odot}} \right)^{-1.5} \left(\frac{R_{core}}{0.1\,\mathrm{pc}} \right)^2 \mathrm{cm^2\ s^{-1}}, \tag{2}$$

where R_{core} is the core radius (see Hueso & Guillot 2005). Precise values for the initial scaling radius are uncertain (see below), but we can estimate upper limits on the j values since $R_1 \leq R_c$ by definition (see Paper I). Substituting $R_1 = R_c$, $R_{core} = 0.1\,\mathrm{pc}$, and the stellar masses in Table 3 into Eq. (2), we find $\log j \approx 19.7\text{-}20.9$ in units of $\mathrm{cm^2\,s^{-1}}$. Radio observations of rotating molecular cloud cores have been used to infer similar or higher values, $\log j \approx 19.6\text{-}22.2$ (Goodman et al. 1993; Barranco & Goodman 1998; Caselli et al. 2002). However, recent numerical simulations have demonstrated that those measurements tend to overestimate j by roughly an order of magnitude (Dib et al. 2010). If that is the case, then the range of disk angular momenta inferred here are actually in good quantitative agreement with those determined for analogs of their parental molecular cloud cores. The low end of the j distribution postulated by Dib et al. (2010) and not probed here could then be explained by a selection effect (perhaps our flux-limited sample only recovers disks with large j values), an unspecified mechanism for angular momentum loss (e.g., outflows or magnetic braking), and/or that $R_1 \ll R_c$ in at least some cases.

Unfortunately, an unambiguous explanation of the *shape* of the M_d-R_c correlation in this scenario is not possible, due to the fundamental degeneracy between the initial disk structures and the rates at which they evolve. The values of M_d and R_c change with time such that $M_d = M_{d,0}/\mathcal{T}^{1/2(2-\gamma)}$ and $R_c = R_1 \mathcal{T}^{1/(2-\gamma)}$, where $M_{d,0}$ and R_1 were the initial disk mass and characteristic radius, respectively, and $\mathcal{T}$ is a dimensionless parameter that tracks how many viscous timescales (t_s) have elapsed, $\mathcal{T} = 1 + t/t_s$ (see Paper I; Hartmann et al. 1998). That evolution is described by 2 equations with 3 unknown parameters, $\{M_{d,0},\ R_1,\ t_s\}$: the evolution rate can not be uniquely disentangled from the initial conditions. However, the lack of significant outliers to the correlation may be related to the viscous evolution process itself. The "small and massive" region in the upper left of Figure 10 is depopulated because these disks spend only a short time with such compact density configurations early in their evolution ($t \ll 1\,\mathrm{Myr}$). Likewise, the "large and low-mass" region to the lower right in this parameter-space is empty because these $\sim 1\,\mathrm{Myr}$-old disks simply have not had enough time to evolve into it.

Alternatively, the inferred M_d-R_c correlation could be the result of coupling the viscous evolution scenario described above with an internal dissipation process. Recent theoretical calculations have suggested that the high-energy (particularly far-ultraviolet, or FUV) irradiation of the disk surface by the central star can drive significant mass loss from large disk radii ($R > 30\,\mathrm{AU}$) in a photoevaporative flow (Gorti & Hollenbach 2009; Gorti et al. 2009). In this scenario, the smaller, low-mass disks in this sample should be associated with an advanced stage in this photoevaporation

process, perhaps because their central stars have more intense FUV radiation fields. Unfortunately, direct constraints on the FUV emission from these extincted sources in the Ophiuchus clouds are rare. Instead, we can approximate the FUV luminosity as the sum of a fraction of the accretion luminosity ($\propto M_* \dot{M}_* / R_*$) and a chromospheric component ($\approx 5 \times 10^{-4} L_*$; see Gorti et al. 2009). However, we find no evidence for an expected anti-correlation between disk masses/sizes and the FUV (or X-ray) luminosities in this sample: if anything, the larger and more massive disks tend to have more intense FUV radiation fields, whereas the less massive, smaller disks show a wide range of FUV luminosities. While this certainly does not exclude a role for photoevaporation in shaping disk structures, it does suggest that diverse initial conditions and viscous timescales are more significant contributors to the observed M_d-R_c correlation at an age of $\sim 1\,\mathrm{Myr}$.

Comparisons of disk properties in different stellar populations will be required to definitively assess the relative impacts that initial conditions, viscous evolution, and dissipation effects like photoevaporation have on shaping disk density distributions over time. The key to disentangling the initial conditions from the viscous evolution timescale is to search for and characterize structural correlations, like the M_d-R_c relationship found here, in disks around stars with a range of ages. In a scenario where viscous evolution dominates, the disks embedded in the envelopes of Class 0/I sources should be massive and compact, providing direct constraints on the distributions of initial masses ($M_{d,0}$) and sizes (R_1). Conversely, the disks in older star-forming regions are expected to be larger and less massive, unless or until FUV photoevaporation can effectively dissipate the mass reservoir in the outer disk. Tracking the evolution of disk masses and sizes in these older stellar populations can provide crucial insights into the distribution of viscous timescales, as well as into the timeframe where photoevaporation may dissipate much of the disk mass reservoir. To probe disk structures in these older star clusters that are typically at larger distances, instruments with increased sensitivity to millimeter continuum emission and access to higher angular resolution will be required. Fortunately, there is great promise for a breakthrough in our understanding of viscous evolution and disk dissipation in the near future, based on extensive millimeter continuum surveys of disk populations with the Atacama Large Millimeter Array (ALMA).

5.2. Implications for Planet Formation

Ultimately, the drive to understand this viscous evolution process lies in the desire to constrain how mass is re-distributed over time, and therefore where and when the conditions in a given disk are suitable for planet formation. All planet formation models require that the disk exceeds some density threshold as a necessary (but perhaps not sufficient) condition for making a planet. In light of the new constraints on disk densities presented here and in Paper I, it is natural to compare them with the two basic recipes for giant planet formation; disk instability (e.g., Boss 1997) and core accretion (e.g., Pollack et al. 1996). In the disk instability model, an over-dense region with a sufficiently short cooling time can fragment out of the global disk structure and precipitate a bound gaseous protoplanet very rapidly ($\sim 10^{3-4}\,\mathrm{yr}$; see the recent review by Durisen et al. 2007).

Typically those conditions are only met at large disk radii (Boley et al. 2006); such protoplanets must then migrate inward to reproduce the shorter period orbits observed in the Solar System and elsewhere. In the core accretion model, a giant planet is produced from a relatively slow ($\sim$1-10 Myr) collisional growth process that first builds up a large solid core and then rapidly accretes a massive gaseous envelope (e.g., Hubickyj et al. 2005; Alibert et al. 2005).

Assuming the dust traces 1% of the gas mass, the disk structures presented here are stable against gravitational fragmentation, with the minimum local Toomre Q values ranging from $\sim$5-50 in most cases ($Q = c_s\Omega/\pi G\Sigma$, where Ω is the Keplerian orbital velocity; Toomre 1964). The large, massive disks around DoAr 25 and GSS 39 are potentially exceptions, with Q values approaching 2 at radii of $\sim$65 and 150 AU, respectively. However, we should caution that the disk structures in both cases are particularly uncertain (see §4.2 of Paper I). While none of the sample disks are clear candidates for the efficient operation of the disk instability mechanism for planet formation in the current epoch (i.e., $Q \leq 1.7$), their structures may have been less stable at earlier times. Even without invoking some kind of mass loading mechanism (Boley 2009), viscous evolution implies that these disks originally had denser, more compact structures, which might suggest a formerly lower minimum Q-value and/or radius where the disk is least stable to fragmentation. A quantitative exploration of the history of $Q(R)$ in these disks grounded in our constraints on their viscous properties may well be worthwhile, but would require new radiative transfer calculations that incorporate some model for the thermal evolution of the disk material in each case.

A similar comparison with the core accretion model is more challenging, primarily because resolution limitations do not yet permit a direct observation of the disk material inside $R \approx 20$ AU. Typically, core accretion model calculations impose a scaled Minimum Mass Solar Nebula (MMSN) density structure for an initial disk, where $\Sigma \propto R^{-3/2}$ (Weidenschilling 1977) and a total mass set to produce a formation efficiency commensurate with the observational constraints on disk lifetimes. Although the MMSN surface density profile is too steep compared to those derived here (where $\Sigma \propto R^{-1}$ at the relevant radii), Figure 6 demonstrates that the surface densities for the sample are generally compatible with those expected in the 20-40 AU region of the primordial Solar disk. The shape of the Σ profile should not adversely affect the likelihood of planet formation if sufficient mass is available, but it is expected to have an impact on the orbital architecture and migration properties of any resulting planetary system (Kokubo & Ida 2002; Chambers & Cassen 2002; Raymond et al. 2005; Crida 2009). Some core accretion simulations have started to employ viscous disk density structures similar to those derived here (e.g., Alibert et al. 2005; Hueso & Guillot 2005), but they still must populate that density structure with solid bodies orders of magnitude larger than those responsible for the observed millimeter emission.

This last point highlights an important uncertainty in deriving densities from observations of young circumstellar disks: the conversion of emission to mass does not account for particles much larger than the observing wavelength. Since this potential for substantially under-estimating the disk densities was already elaborated in Paper I, we will not dwell on it here. The problem is not likely to be severe in the regions that can currently be probed observationally ($R \geq 20$ AU), as

even optimistic estimates of particle growth timescales at those radii do not predict a substantial population of large solids (e.g., Dullemond & Dominik 2005). However, at smaller disk radii those growth timescales can be considerably shorter, generating a dust emissivity that varies with radius inside the planet formation zone. More generally, it is worthwhile to emphasize that the observations are not yet sensitive to the midplane material for $R < 20\,\mathrm{AU}$. Inside that resolution limit, the densities could be dramatically different than inferred here if, for example, the dust size distribution is changed or the effective viscosity profile is modified (e.g., Zhu et al. 2010). New data from ALMA and the Expanded Very Large Array (EVLA) will help alleviate these uncertainties at small radii, and should also help empirically guide our understanding of disk viscosities.

But despite our general ignorance of the inner disk structures, a subset of young disks show unambiguous evidence for evolution in the planet formation zone. In this SMA survey of 17 disks, selected primarily for their millimeter luminosities, 4 of them - around SR 24 S, SR 21, WSB 60, and DoAr 44 - have large central cavities with significantly diminished dust emission. The characteristic ring-like emission morphologies and distinctive visibility nulls for these disks indicate that the radial transition in the millimeter optical depth across the cavity edge is rather sharp, commensurate with our simple models that employ a density contrast of $\sim 10^2$-10^4 within a small radial range. In 3 of these 4 disks, a small amount of micron-sized dust grains must reside inside the cavity to account for their observed infrared excess emission. Outside of their central cavities, these disks have Σ profiles comparable to the disks with continuous dust distributions. At this point, the physical mechanism responsible for the dust evolution in these disk cavities remains a subject of active debate (e.g., see D'Alessio et al. 2005; Najita et al. 2007). They could be produced by an abrupt emissivity decrease due to grain growth in a localized region of low turbulence (e.g., an MRI-inactive "dead" zone; Ciesla 2007; Zhu et al. 2010). Alternatively, they may represent a true lack of material in the inner disk, cleared out by a photoevaporative wind and viscous draining (Alexander & Armitage 2007) or tidal interactions with faint companions - perhaps even young planetary systems (e.g., Lubow & D'Angelo 2006).

6. Summary

We have conducted a high angular resolution (down to FWHM scales of $0.''3 \approx 40\,\mathrm{AU}$) Submillimeter Array survey of the $880\,\mu\mathrm{m}$ continuum emission from 17 protoplanetary disks in the $\sim 1\,\mathrm{Myr}$-old Ophiuchus star-forming region (see also Andrews et al. 2009). Using a two-dimensional parametric model for the structure of a viscous accretion disk and a Monte Carlo radiative transfer code to simultaneously reproduce the millimeter visibilities and broadband SEDs, we have measured the spatial distribution of mass in these disks. The key conclusions from this survey include:

1. Assuming the viscosity scales with radius like a power-law ($\nu \propto R^\gamma$) and the surface densities like $\Sigma \propto (R/R_c)^{-\gamma} \exp\left[-(R/R_c)^{2-\gamma}\right]$, the disks in this survey exhibit a relatively narrow range of density/viscosity gradients, $\gamma = 0.4$-1.1. Taken together as a sample, these results

are consistent with a single (median) value, $\langle\gamma\rangle = 0.9 \pm 0.2$, independent of the millimeter luminosity (disk mass) or the stellar properties.

2. The disk masses (M_d) and characteristic radii (R_c) are correlated: massive disks tend to be larger (i.e., brighter disks are more resolved). The $3.3\,\sigma$ correlation is described well by a power-law relation, $M_d \propto R_c^{1.6\pm0.3}$ (with a residual scatter of $\sim$0.3 dex). Rough estimates of the range of angular momenta in these disks are found to be comparable to the values inferred for rotating molecular cloud cores. If it can be measured in disk samples with a well-established range of ages, the M_d-R_c relationship can be used to deduce a mean viscous timescale and the range of initial conditions imparted by the disk formation process.

3. Based on the derived physical conditions in these disks and literature measurements of their mass accretion rates, we have made crude estimates of their viscosity coefficients (α; Shakura & Sunyaev 1973). The inferred α values range from 0.0005-0.08, with a median $\langle\alpha\rangle \approx 0.01$. This range of values is commensurate with numerical simulations where the effective viscosities are generated by turbulence from the magnetorotational instability in slightly ionized disks.

4. The inferred disk surface densities in the $\sim$20-40 AU range are in good quantitative agreement with those expected for the primordial disk that gave rise to the giant planets Uranus and Neptune (i.e., the outer part of the Minimum Mass Solar Nebula). Current limitations on angular resolution prevent more direct constraints on Σ in the inner disk ($R < 20$ AU). All of the sample disks appear to be gravitationally stable (typical minimum Toomre Q values range from $\sim$5-50). However, these results do not rule out periods where the disk instability mechanism for planet formation at earlier epochs ($\ll 1$ Myr).

5. Regions of significantly diminished millimeter emission were resolved at the centers of 4/17 disks in the sample (SR 24 S, SR 21, DoAr 44, and WSB 60). Simple models for these "transition" disks can reproduce the observations well if the densities are decreased by a factor of $\geq$100 inside a radius $R_{\rm cav} \approx$ 20-40 AU. The disk properties outside these central cavities are comparable to the other disks in the sample. The significant infrared excesses still present in 3/4 of these disks with resolved central cavities indicate that some small, warm, dust particles remain near their central stars. The implied dust structures in those cases are commensurate with the opening of large gaps in the planet formation zones of these disks.

Table 1.   SMA Observing Journal

Name (1)	α [J2000] (2)	δ [J2000] (3)	Array (4)	UT Date (5)	Alt. Name (6)
Elias 24	16 26 24.08	−24 16 13.7	V	2009 March 14	WSB 31, YLW 32
			C	2009 May 2	
SR 24 S	16 26 58.51	−24 45 37.0	V	2009 March 25	DoAr 29, Haro 1-7
			C	2009 May 4	
SR 4	16 25 56.16	−24 20 48.5	V	2009 March 12	V2058 Oph, AS 206
			V	2009 March 25	
			C	2009 May 4	
SR 13	16 28 45.27	−24 28 19.2	V	2009 March 12	V853 Oph, HBC 266
			C	2009 May 2	
WSB 52	16 27 39.44	−24 39 15.7	V	2009 March 2	ROXs 27
			V	2009 March 28	
			C	2009 May 4	
DoAr 33	16 27 39.01	−23 58 18.9	V	2009 March 2	WSB 53, ROXs 30C
			V	2009 March 28	
			C	2009 May 4	
WL 18	16 26 48.98	−24 38 25.4	V	2009 March 13	GY 129
			C	2009 May 2	
DoAr 24 E	16 26 23.37	−24 20 59.8	V	2009 March 13	Elias 22, GSS 31
			C	2009 May 2	

Note. — Col. (1): Disk name. Cols. (2) & (3): Centroid coordinates, determined as described in the text (§2). The coordinates listed for DoAr 24 E correspond to the optically-visible component to the northwest. Col. (4): Array configuration; V = very extended (68-509 m baselines) and C = compact (16-70 m baselines). Col. (5): UT date of observation. Col. (6): Common alternative identifications.

Table 2.   Continuum and CO Synthesized Map Properties

Disk	continuum			CO $J=3-2$		
	F_ν	θ_b	PA$_b$	rms	θ_b	PA$_b$
	[mJy]	['']	[°]	[Jy]	['']	[°]
(1)	(2)	(3)	(4)	(5)	(6)	(7)
Elias 24	890 ± 3	0.65×0.51	18	0.19	2.13×1.42	51
SR 24 S	545 ± 3	0.51×0.43[a]	89	0.25	2.15×1.44	52
SR 4	150 ± 2	0.50×0.43	15	0.24	2.12×1.45	53
SR 13	149 ± 3	0.63×0.52	39	0.19	2.15×1.41	50
WSB 52	147 ± 3	0.50×0.43	52	0.25	2.16×1.44	52
DoAr 33	80 ± 2	0.52×0.43	67	0.25	2.17×1.42	53
WL 18	51 ± 3	0.61×0.52	55	0.19	2.19×1.39	50
DoAr 24 E	49 ± 2[b]	0.60×0.54	58	0.19	2.21×1.37	50

Note. — Col. (1): Disk name. Col. (2): Integrated continuum flux density and rms noise level per beam (does not include the ∼10% flux calibration uncertainty). Cols. (3) & (4): FWHM dimensions and position angle (measured east of north) of the synthesized beam for the continuum maps shown in Figure 2. Col. (5): The rms noise level per beam for an individual $0.70\,\mathrm{km\,s}^{-1}$ channel in the synthesized CO $J=3-2$ channel maps. Cols. (6) & (7): FWHM dimensions and position angle of the synthesized beam for the channel maps.

[a]The high-resolution inset map of the SR 24 S disk shown in Figure 2 was generated with uniform visibility weighting and has a synthesized beam with dimensions $0\rlap{.}''37 \times 0\rlap{.}''26$ at PA $= 14°$.

[b]The infrared companion source to the southeast is just slightly fainter, with an integrated flux density of $34 \pm 2\,\mathrm{mJy}$.

Table 3.   Stellar Properties

Name	SpT	A_V [mag]	$T_{\rm eff}$ [K]	R_* [$R_\odot$]	L_* [$L_\odot$]	M_* [$M_\odot$]	age [Myr]	ref
(1)	(2)	(3)	(4)	(5)	(6)	(7)	(8)	(9)
AS 205	K5	2.9	4250	3.7	4.0	1.0	0.5	1
Elias 24	K5	8.7	4250	4.2	5.1	1.0	0.4	2
GSS 39	M0	15	3850	2.3	1.0	0.6	1.0	3
AS 209	K5	0.9	4250	2.3	1.5	0.9	1.6	4
DoAr 25	K5	2.7	4250	1.7	0.8	1.0	3.8	2
SR 24 S	K2	7.0	4990	2.8	4.4	2.0	2.4	3
WaOph 6	K6	3.6	4205	3.2	2.9	0.9	0.7	5
SR 21	G3	6.3	5800	3.3	11	2.0	4.7	1
VSSG 1	M0	14	3850	3.1	1.9	0.6	0.7	6
WSB 60	M4	3.5	3370	1.3	0.2	0.3	3.0	2
DoAr 44	K3	2.3	4730	1.7	1.3	1.4	7.1	7
SR 4	K7	1.3	4060	2.0	1.0	0.7	1.8	3
SR 13	M4	0.0	3370	1.9	0.4	0.3	1.5	2
WSB 52	M1	5.0	3750	1.9	0.6	0.5	1.5	3
DoAr 33	K4	3.7	4470	1.8	1.2	1.3	4.4	7
WL 18	K7	11	4060	1.1	0.3	0.8	11	2

Note. — Col. (1): Disk name (those in italics were modeled in Paper I). Col. (2): Spectral type. Col. (3): Extinction. Col. (4): Effective temperature. Col. (5): Radius. Col. (6): Luminosity. Col. (7) and (8): Mass and age estimated from the Siess et al. (2000) pre-main-sequence models. Col. (9): Literature references for SpT and A_V: [1] - Prato et al. (2003), [2] - Wilking et al. (2005), [3] - Luhman & Rieke (1999), [4] - Herbig & Bell (1988), [5] - Eisner et al. (2005), [6] - Natta et al. (2006), [7] - Bouvier & Appenzeller (1992).

Table 4.   Disk Structure Model Parameters: Continuous Cases

Name	M_d [M$_\odot$]	γ	R_c [AU]	H_{100} [AU]	ψ	$R_{\rm in}$ [AU]	i [°]	PA [°]	$\tilde{\chi}^2_{\rm vis}$	$\tilde{\chi}^2_{\rm sed}$
(1)	(2)	(3)	(4)	(5)	(6)	(7)	(8)	(9)	(10)	(11)
AS 205	0.029	0.9	46	19.6	0.11	0.14	25	165	2.1	3.7
Elias 24	0.117	0.9	127	8.6	0.03	0.16	24	50	2.0	1.5
GSS 39	0.143	0.7	198	7.3	0.08	0.07	60	110	1.9	32
AS 209	0.028	0.4	126	13.3	0.10	0.09	38	86	1.7	2.4
DoAr 25	0.136	0.9	80	6.7	0.15	0.06	59	112	1.9	9.2
WaOph 6	0.077	1.0	153	4.4	0.06	0.12	39	171	1.8	1.8
VSSG 1	0.029	0.8	33	9.7	0.08	0.10	53	165	1.8	12
SR 4	0.004	0.8	20	19.9	0.23	0.07	50	39	1.9	8.8
SR 13	0.012	1.0	26	12.6	0.07	0.04	32	42	2.0	1.9
WSB 52	0.007	1.1	26	14.5	0.19	0.06	46	120	1.9	6.6
DoAr 33	0.007	1.1	38	2.7	0.06	0.07	43	102	1.9	22
WL 18	0.011	0.8	14	5.6	0.07	0.04	48	115	1.9	13

Note. — Col. (1): Disk name (those in italics were modeled in Paper I). Col. (2): Disk mass assuming a 100:1 gas-to-dust mass ratio. Col. (3): Radial surface density gradient. Col. (4): Characteristic radius. Col. (5): Scale height at 100 AU. Col. (6): Radial scale height gradient. Col. (7): Fixed inner radius. Col. (8): Fixed inclination. Col. (9): Fixed major axis position angle. Col. (10): Reduced χ^2 statistic comparing the model fit with the continuum visibilities alone. Col. (11): Same as Col. (10), but for the SED alone.

Table 5.   Disk Structure Model Parameters: Central Cavity Cases

Name	M_d [M$_\odot$]	γ	R_c [AU]	H_{100} [AU]	ψ	R_{cav} [AU]	δ_{cav}	i [°]	PA [°]	$\tilde{\chi}^2_{\mathrm{vis}}$	$\tilde{\chi}^2_{\mathrm{sed}}$
(1)	(2)	(3)	(4)	(5)	(6)	(7)	(8)	(9)	(10)	(11)	(12)
SR 24 S	0.042	0.8	40	4.0	0.02	32	0.0001	57	31	2.1	11
SR 21	0.005	0.9	17	7.7	0.26	37	0.005	22	110	1.7	7.2
WSB 60	0.021	0.8	31	11.0	0.13	20	0.01	25	117	1.8	3.0
DoAr 44	0.017	1.0	80	3.5	0.04	33	0.0001	45	75	1.8	$\cdots$

Note. — Cols. (1-6): Same as for Table 4. Col. (7): The cavity radius, marking the outer edge of the diminished inner disk densities (see Paper I or the discussion on SR 24 S in §4.2). Col. (8): The density reduction scaling factor inside the radius R_{cav}. Cols. (9-12): Same as for Table 4 cols. (8-11).

Table 6.   Viscous Disk Properties

Name	$\dot{M}_*$	R_t	α	ref
	[$M_\odot$ yr^{-1}]	[AU]		
(1)	(2)	(3)	(4)	(5)
AS 205	8×10^{-8}	23	0.005	1
Elias 24	2×10^{-7}	62	0.03	2
GSS 39	7×10^{-8}	95	0.03	2
AS 209	9×10^{-8}	61	0.08	3
DoAr 25	3×10^{-9}	39	0.0005	4
WaOph 6	1×10^{-7}	78	0.05	5
VSSG 1	1×10^{-7}	16	0.02	2
SR 4	6×10^{-8}	10	0.02	2
SR 13	3×10^{-9}	13	0.0005	2
WSB 52	4×10^{-9}	13	0.001	2
DoAr 33	3×10^{-10}	20	0.0006	6
WL 18	9×10^{-9}	7	0.003	2
SR 24 S	3×10^{-8}	19	(0.006)	2
SR 21	$< 2 \times 10^{-9}$	9	(<0.0009)	2
WSB 60	1×10^{-9}	15	(0.0002)	2
DoAr 44	9×10^{-9}	40	(0.01)	7

Note. — Col. (1): Disk name (those in italics were modeled in Paper I). Col. (2): Accretion rate. Col. (3): Radius of mass flow reversal. Col. (4): Viscosity coefficient. Col. (5): References for $\dot{M}_*$: [1] - Prato et al. (2003), [2] - Natta et al. (2006), [3] - Johns-Krull et al. (2000), [4] - Luhman & Rieke (1999), [5] - Eisner et al. (2005), [6] - Cieza et al. (2010), [7] - Espaillat et al. (2010).
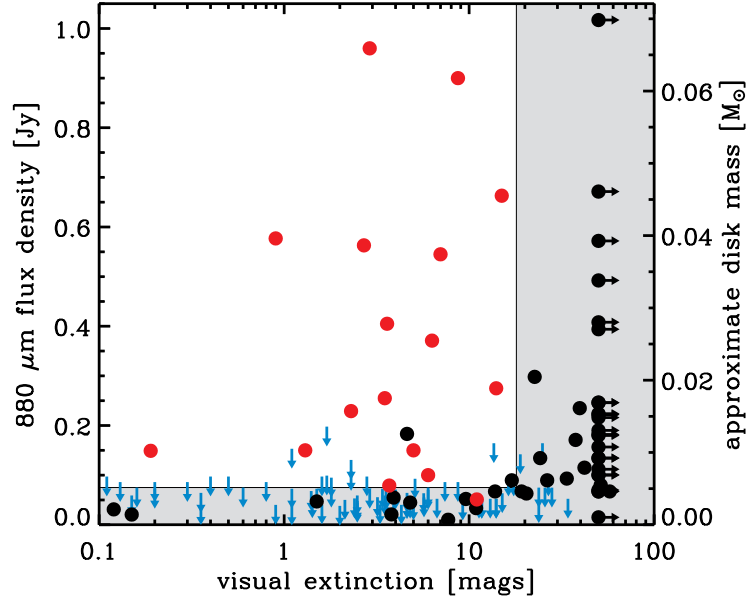
Fig. 1.— The millimeter continuum flux densities and visual extinctions for young stars in the Ophiuchus molecular clouds (Andrews & Williams 2007a,b; Cieza et al. 2010; additional A_V estimates from Furlan et al. 2009). The targets selected for this sample are shown in red ($880\,\mu$m flux densities are from Table 2 and Paper I), and the regions that do not meet the selection criteria are shaded grey. Blue arrows represent $3\,\sigma$ upper limits and black points mark sources that have not been observed with the SMA at high angular resolution. Embedded sources with uncertain spectral classifications are represented with a lower limit of $A_V = 50$. When $880\,\mu$m flux densities are not available, $1.3\,$mm data were scaled up by a factor of $\sim$2.2 (see text); the right-hand ordinate axis represents an approximate conversion of the flux density scale to total disk masses (see Andrews & Williams 2005; 2007b).
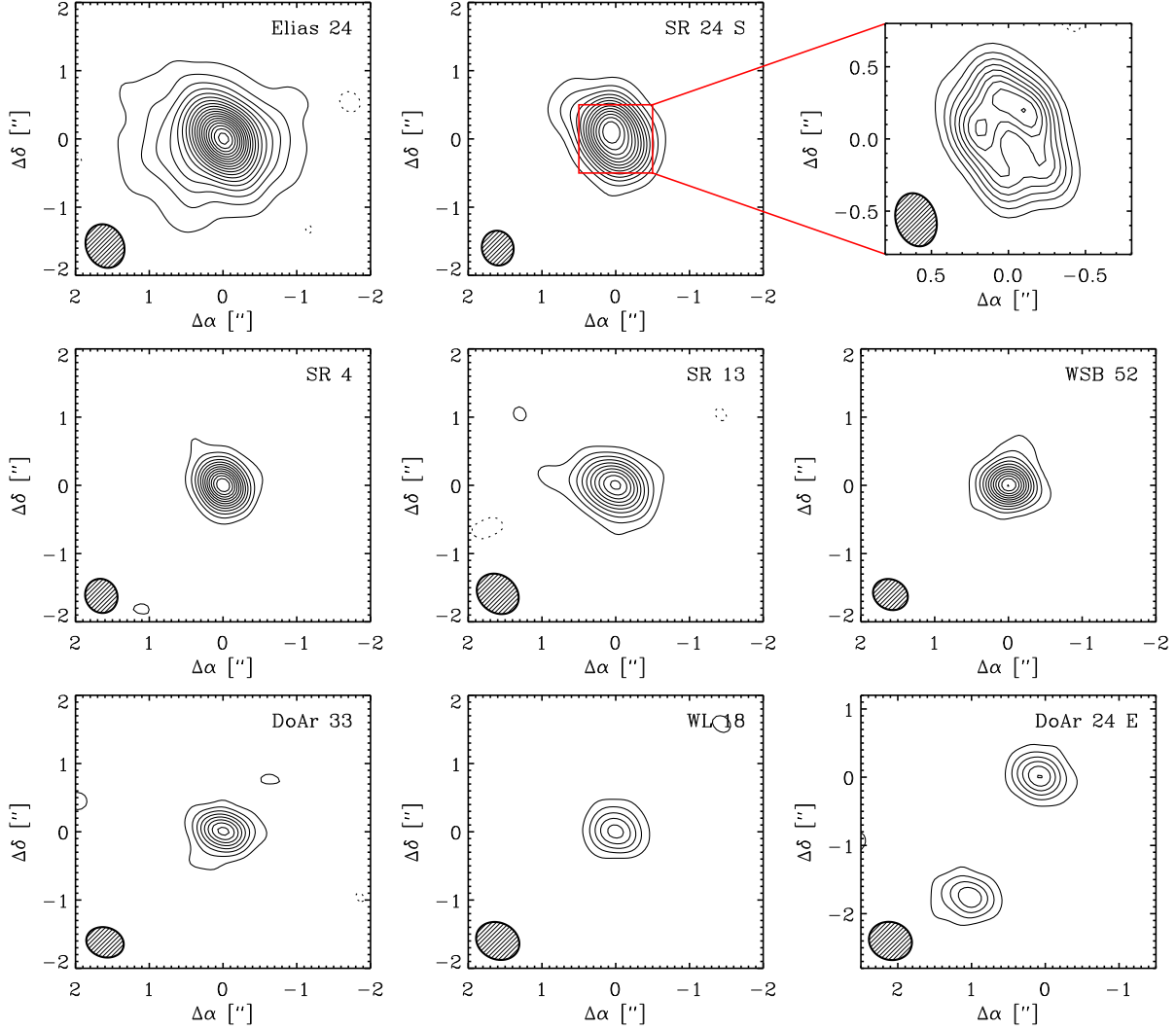
Fig. 2.— Aperture synthesis images of the $880\,\mu$m continuum emission from the 8 disk targets in the expanded sample. Each panel is $4''$ (500 AU) on a side. Contours start at $3\,\sigma$ and increase in $3\,\sigma$ intervales ($5\,\sigma$ for Elias 24 and SR 24 S only; rms values are given in Table 2). The synthesized beams are shown in the lower left corner of each panel. Note the detection of roughly equal emission levels around both the optically-visible primary star DoAr 24 E and its infrared companion to the southeast, as well as the asymmetric ring-like emission morphology for the disk around SR 24 S (shown separately in detail).
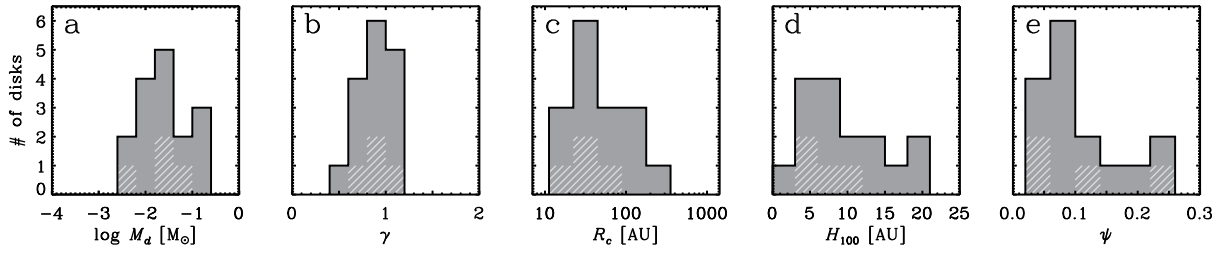
Fig. 3.— The derived distributions of the disk structure parameters for the composite sample (combining the results presented here and in Paper I). From left to right are the disk masses (M_d), radial surface density gradients (γ), characteristic radii (R_c), scale-heights at 100 AU (H_{100}), and the radial scale-height gradients (ψ). The contributions of the four disks with diminished millimeter emission in their central regions are hatched.
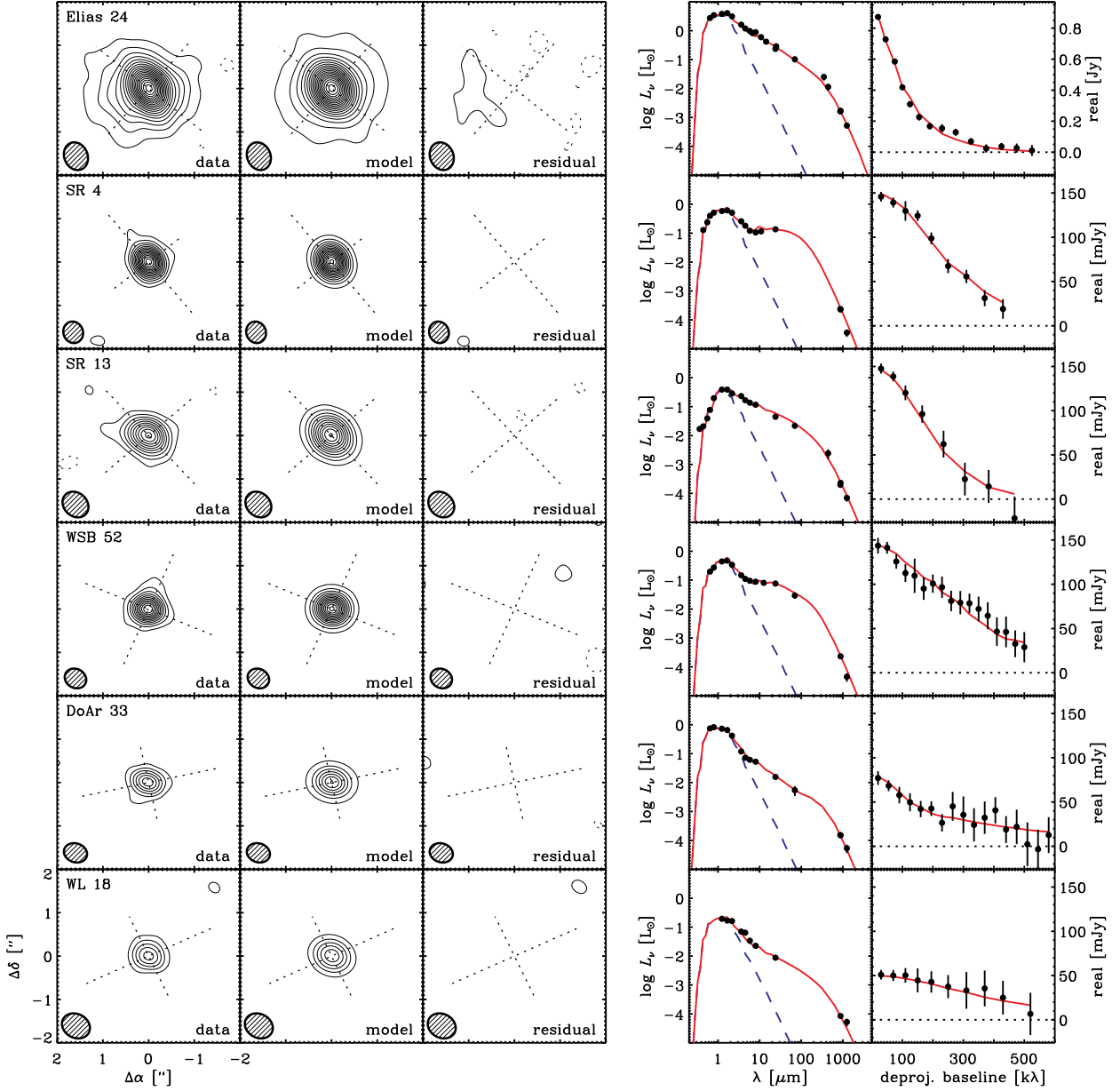
Fig. 4.— Comparison of the data with the best-fit disk structure models. The left panels show the SMA continuum image, corresponding model image, and imaged residuals (data−model). Contours are drawn at the same $3\,\sigma$ intervals in each panel. Crosshairs mark the disk centers and major axis position angle; their relative lengths represent the disk inclination. The right panels show the broadband SEDs and deprojected visibility profiles, with best-fit models overlaid in red. The input stellar photospheres are shown as blue dashed curves.
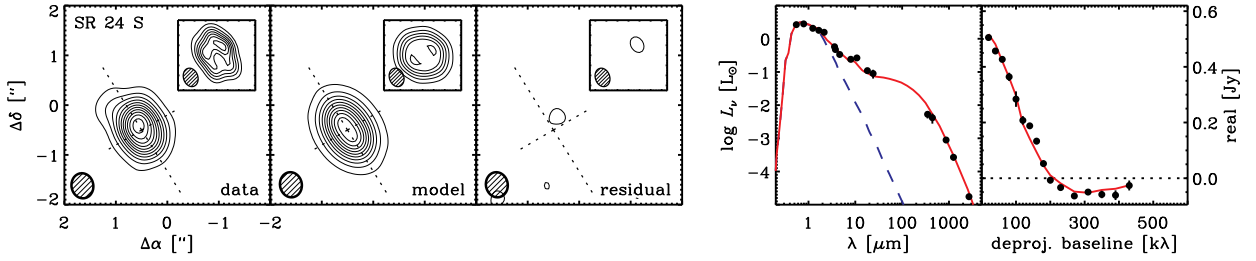
Fig. 5.— Same as Figure 4 for the SR 24 S disk, which features a resolved central emission cavity. The modifications to the standard disk model made for this source in particular are detailed in §4.2. The inset images are to scale, and were synthesized by uniformly weighting the visibilities to highlight the structure at higher angular resolution.
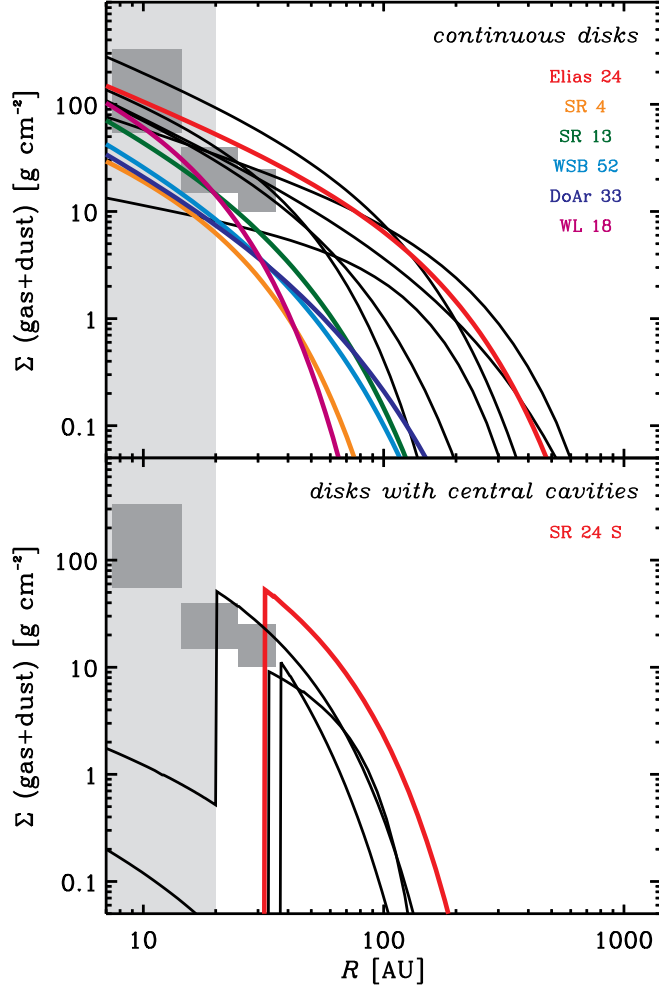
Fig. 6.— Surface density profiles for the sample, where the targets with continuous emission distributions (*top*) and central emission cavities (*bottom*) are separated for clarity. The new model results presented here are highlighted in color, while those from Paper I are shown in black. The light grey band out to a radius of 20 AU marks the resolution limit of the survey. Dark gray boxes represent the surface densities extrapolated for Saturn, Uranus, and Neptune in the standard Minimum Mass Solar Nebula (Weidenschilling 1977). The density profiles inferred from dust tracers have been scaled up assuming a gas-to-dust mass ratio of 100:1.
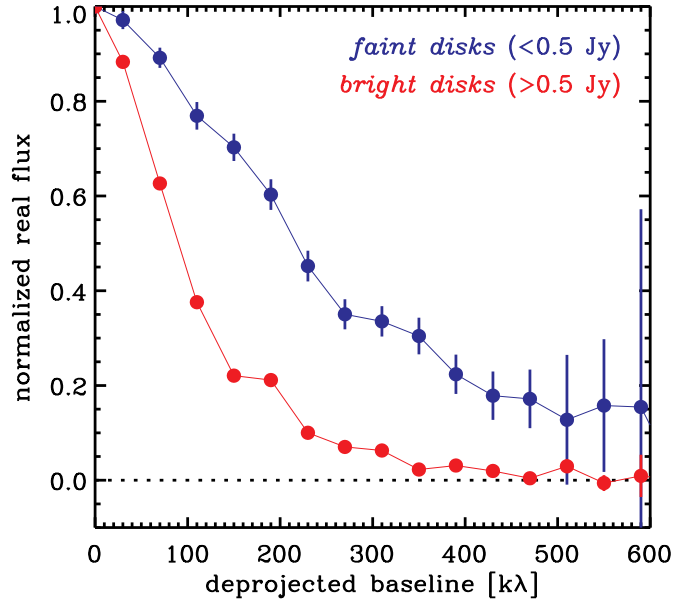
Fig. 7.— A direct comparison of the sample-averaged visibility profiles for the subsets of disks with integrated $880\,\mu$m flux densities fainter (*blue*) and brighter (*red*) than 0.5 Jy. Each profile was constructed by averaging the visibilities for individual disks in annular bins after their deprojection according to viewing geometry and normalization by their total flux densities. The disks with large central emission cavities were excluded for clarity. Error bars correspond to the standard deviation in each bin. The significantly larger amount of correlated emission on all spatial scales for the fainter subset of disks demonstrates that they are less well resolved, and therefore substantially smaller than their brighter counterparts. This empirical relationship is reinforced by the radiative transfer modeling, which implies a modest correlation between M_d and R_c (see §5.1).
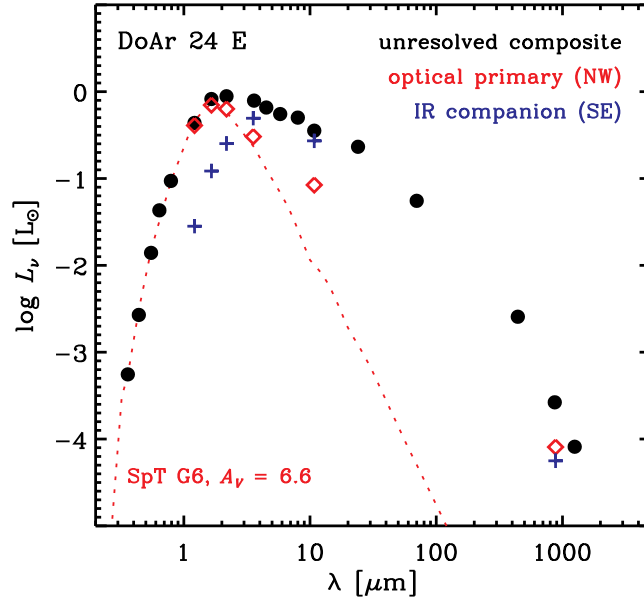
Fig. 8.— The SED for the combined DoAr 24 E system (*black circles*) is shown together with the component-resolved SEDs of the optical primary (*red*) and infrared companion (*blue*) that lie to the northwest and southeast in Figure 2, respectively. A model stellar photosphere for the optical primary is shown as a dashed red curve. Unlike those shown in Figure 4, these SEDs have not been corrected for extinction due to the uncertainty in the nature of the infrared companion source.
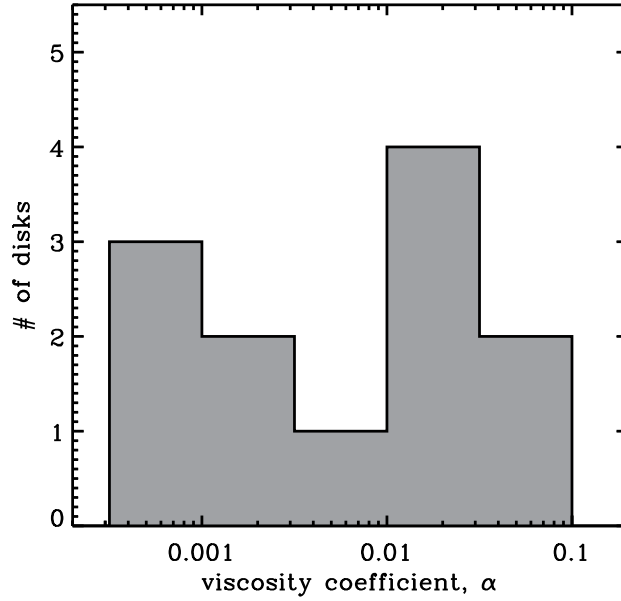
Fig. 9.— The distribution of viscosity coefficients, α, inferred for this sample from the disk structures and mass accretion rates. The individual α values listed in Table 6 are still quite uncertain, although the broad range is commensurate with simulations where the disk viscosities are sustained by MHD turbulence. Given the small sample size, α uncertainties, and potential $\dot{M}_*$ bias, the bimodal appearance of the distribution is not significant.

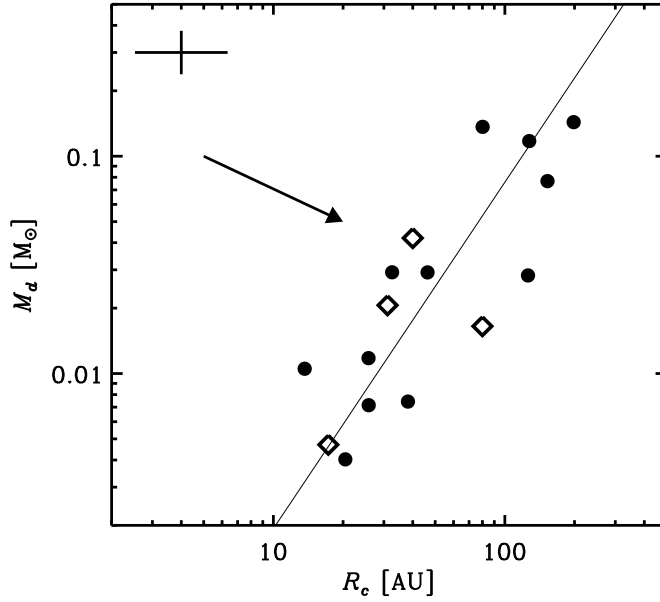Fig. 10.— A $3.3\,\sigma$ correlation between the disk masses and characteristic radii. The solid line shows a power-law that provides a reasonable match to this relationship, where $M_d \propto R_c^x$ with $x = 1.6 \pm 0.3$. Diamond symbols mark the disks with large central emission cavities, and the cross to the upper left is representative of the typical parameter uncertainties. The arrow denotes the generic direction of evolution implied by the conservation of angular momentum. The range along the correlation is representative of the range of angular momenta incorporated into the disks when they formed, but the shape of the correlation encodes both these initial conditions and potentially a range of viscous timescales.

REFERENCES

Alexander, R. D., & Armitage, P. J. 2007, MNRAS, 375, 500

Alibert, Y., Mordasini, C., Benz, W., & Winisdoerffer, C. 2005, A&A, 434, 343

André, P., & Montmerle, T. 1994, ApJ, 420, 837

Andrews, S. M., & Williams, J. P. 2005, ApJ, 619, L175 (2005a)

———— 2005, ApJ, 635, 1134 (2005b)

———— 2007, ApJ, 659, 705 (2007a)

———— 2007, ApJ, 671, 1800 (2007b)

Andrews, S. M., Wilner, D. J., Hughes, A. M., Qi, C., & Dullemond, C. P. 2009, ApJ, 700, 1502 (Paper I)

Barranco, J. A., & Goodman, A. A. 1998, ApJ, 504, 207

Barsony, M., Ressler, M. E., & Marsh, K. A. 2005, ApJ, 630, 381

Beckwith, S. V. W., Sargent, A. I., Chini, R. S., & Güsten, R. 1990, AJ, 99, 924

Boley, A. C., Mejía, A. C., Durisen, R. H., Cai, K., Pickett, M. K., & D'Alessio, P. 2006, ApJ, 651, 517

Boley, A. C. 2009, ApJ, 695, L53

Bontemps, S., et al. 2001, A&A, 372, 173

Boss, A. P. 1997, Science, 276, 1836

Bouvier, J., & Appenzeller, I. 1992, A&AS, 92, 481

Brown, J. M., Blake, G. A., Qi, C., Dullemond, C. P., & Wilner, D. J. 2008, ApJ, 675, L109

Brown, J. M., Blake, G. A., Qi, C., Dullemond, C. P., Wilner, D. J., & Williams, J. P. 2009, ApJ, 704, 496

Caselli, P., Benson, P. J., Myers, P. C., & Tafalla, M. 2002, ApJ, 572, 238

Chambers, J. E., & Cassen, P. 2002, Meteoritics & Planetary Science, 37, 1523

Chiang, E. I., & Goldreich, P. 1997, ApJ, 490, 368

Ciesla, F. J. 2007, ApJ, 654, L159

Cieza, L. A., et al. 2010, ApJ, 712, 925

Crida, A. 2009, ApJ, 698, 606

Cutri, R. M., et al. 2003, 2MASS All-Sky Point Source Catalog (Pasadena: IPAC)

D'Alessio, P. et al. 2005, ApJ, 621, 461

Dartois, E., Dutrey, A., & Guilloteau, S. 2003, A&A, 399, 773

de Geus, E. J., de Zeeuw, P. T., & Lub, J. 1989, A&A, 216, 44

Dib, S., Hennebelle, P., Pineda, J. E., Csengeri, T., Bontemps, S., Audit, E., & Goodman, A. A. 2010, ApJ, in press (arXiv:1003.5118)

Draine, B. T., & Lee, H. M. 1984, ApJ, 285, 89

Dullemond, C. P., & Dominik, C. 2004, A&A, 417, 159

——— 2005, A&A, 434, 971

Durisen, R. H., Boss, A. P., Mayer, R. L., Nelson, A. F., Quinn, T., & Rice, W. K. M. 2007, in Protostars & Planets V, eds. B. Reipurth, D. Jewitt, & K. Keil (Tucson: Univ. Arizona Press), 607

Eisner, J. A., Hillenbrand, L. A., White, R. J., Akeson, R. L., & Sargent, A. I. 2005, ApJ, 623, 952

Espaillat, C., et al. 2007, ApJ, 670, L135

——— 2010, ApJ, in press (arXiv:1005.2365)

Evans, N. J., et al. 2003, PASP, 115, 965

Fleming, T., & Stone, J. M. 2003, ApJ, 585, 908

Fromang, S., Papaloizou, J., Lesur, G., & Heinemann, T. 2007, A&A, 476, 1123

Furlan, E., et al. 2009, ApJ, 703, 1964

Garaud, P. 2007, ApJ, 671, 2091

Ghez, A. M., Neugebauer, G., & Matthews, K. 1993, AJ, 106, 2005

Goodman, A. A., Benson, P., Fuller, G., & Myers, P. 1993, ApJ, 406, 528

Gorti, U., & Hollenbach, D. 2009, ApJ, 690, 1539

Gorti, U., Dullemond, C. P., & Hollenbach, D. 2009, ApJ, 705, 1237

Gullbring, E., & Calvet, N. 1998, ApJ, 509, 802

Gullbring, E., Calvet, N., Muzerolle, J., & Hartmann, L. 2000, ApJ, 544, 927

Hartmann, L., Calvet, N., Gullbring, E., & D'Alessio, P. 1998, ApJ, 495, 385

Hawley, J. F., Gammie, C. F., & Balbus, S. A. 1995, ApJ, 440, 742

Herbig, G. H., & Bell, K. R. 1988, in Third Catalog of Emission Line Stars of the Orion Population (Santa Cruz: Lick Obs.)

Herbst, W., Herbst, D. K., & Grossman, E. J. 1994, AJ, 108, 1906

Hillenbrand, L. A. 2009, in IAU Symp. 258, The Age of Stars, ed. E. Mamajek, et al. (Cambridge: Cambridge University Press), 81

Ho, P. T. P., Moran, J. M., & Lo, K. Y. 2004, ApJ, 616, L1

Hubickyj, O., Bodenheimer, P., & Lissauer, J. J. 2005, Icarus, 179, 415

Hueso, R., & Guillot, T. 2005, A&A, 442, 703

Hughes, A. M., Wilner, D. J., Calvet, N., D'Alessio, P., Claussen, M. J., & Hogerheijde, M. R. 2007, ApJ, 664, 536

Hughes, A. M., Wilner, D. J., Qi, C., & Hogerheijde, M. R. 2008, ApJ, 678, 1119

Hughes, A. M., et al. 2009, ApJ, 698, 131

Ida, S., & Lin, D. N. C. 2004, ApJ, 604, 388

Isella, A., Carpenter, J. M., & Sargent, A. I. 2009, ApJ, 701, 260

——— 2010, ApJ, 714, 1746

Jensen, E. L. N., & Mathieu, R. D. 1997, AJ, 114, 301

Johns-Krull, C. M., Valenti, J. A., & Linsky, J. L. 2000, ApJ, 539, 815

Kitamura, Y., Momose, M., Yokogawa, S., Kawabe, R., Tamura, M., & Ida, S. 2002, ApJ, 581, 357

Kokubo, E., & Ida, S. 2002, ApJ, 581, 666

Knude, J., & Høg, E. 1998, A&A, 338, 897

Loinard, L., Torres, R. M., Mioduszewski, A. J., & Rodríguez, L. F. 2008, ApJ, 675, L29

Lombardi, M., Lada, C. J., & Alves, J. 2008, A&A, 480, L785

Lubow, S. H., & D'Angelo, G. 2006, ApJ, 641, 526

Luhman, K. L., & Rieke, G. H. 1999, ApJ, 525, 440

Lynden-Bell, D., & Pringle, J. E. 1974, MNRAS, 168, 603

Mayama, S., et al. 2010, Science, 327, 306

McCabe, C., Ghez, A. M., Prato, L., Duchene, G., Fischer, R. S., & Telesco, C. 2006, ApJ, 636, 932

McCaughrean, M. J., & O'Dell, C. R. 1996, AJ, 111, 1977

Mordasini, C., Alibert, Y., & Benz, W. 2009, A&A, 501, 1139

Motte, F., André, P., & Neri, R. 1998, A&A, 336, 150

Muzerolle, J., Calvet, N., & Hartmann, L. 1998, ApJ, 492, 743

Muzerolle, J., Hartmann, L., & Calvet, N. 1998, AJ, 116, 2965 (1998b)

Natta, A., Testi, L., & Randich, S. 2006, A&A, 452, 245

Najita, J. R., Strom, S. E., & Muzerolle, J. 2007, MNRAS, 378, 369

Nürnberger, D., Brandner, W., Yorke, H. W., & Zinnecker, H. 1998, A&A, 330, 549

Padgett, D. C., et al. 2008, ApJ, 672, 1013

Patience, J., Akeson, R. L., & Jensen, E. L. N. 2008, ApJ, 677, 616

Piétu, V., Dutrey, A., Guilloteau, S., Chapillon, E., & Pety, J. 2006, A&A, 460, L43

Piétu, V., Dutrey, A., & Guilloteau, S. 2007, A&A, 467, 163

Pollack, J. B., Hubickyj, O., Bodenheimer, P., Lissauer, J. J., Podolak, M., & Greenzweig, Y. 1996, Icarus, 124, 62

Prato, L., Greene, T. P., & Simon, M. 2003, ApJ, 584, 853

Raymond, S. N., Quinn, T., & Lunine, J. I. 2005, ApJ, 632, 670

Reipurth, B., & Zinnecker, H. 1993, A&A, 278, 81

Schaefer, G. H., Simon, M., Beck, T. L., Nelan, E., & Prato, L. 2006, AJ, 132, 2618

Shakura, N. I., & Sunyaev, R. A. 1973, A&A, 24, 337

Siess, L., Dufour, E., & Forestini, M. 2000, A&A, 358, 593

Simon, M., et al. 1995, ApJ, 443, 625

Stanke, T., Smith, M. D., Gredel, R., & Kanzadyan, T. 2006, A&A, 447, 609

Stone, J. M., Hawley, J. F., Gammie, C. F., & Balbus, S. A. 1996, ApJ, 463, 656

Toomre, A. 1964, ApJ, 139, 1217

Weidenschilling, S. J. 1977, Ap&SS, 51, 153

Weingartner, J. C., & Draine, B. T. 2001, ApJ, 548, 296

Wilking, B. A., Meyer, M. R., Robinson, J. G., & Greene, T. P. 2005, AJ, 130, 1733

Zhu, Z., Hartmann, L., & Gammie, C. 2010, ApJ, 713, 1143